Toward New 2D Zirconium-Based Metal–Organic Frameworks: Synthesis, Structures, and Electronic Properties

Towards new 2D zirconium-based metal–organic frameworks: synthesis, structures and electronic properties

Amandine Cadiau, [†,⊥] Lilia S. Xie, [‡] Nikita Kolobov, [†] Aleksander Shkurenko, [§] Muhammad Qureshi, [⊥] Mohamed R. Tchalala, [§] Sarah S. Park, [‡] Anastasiya Bavykina, [†] Mohamed Eddaoudi, [§] Mircea Dincă, [‡] Christopher H. Hendon, [∥] Jorge Gascon *[†]

[†] King Abdullah University of Science and Technology, KAUST Catalysis Center (KCC), Advanced Catalytic Materials, Thuwal, 23955-6900, Saudi Arabia

[‡] Department of Chemistry, Massachusetts Institute of Technology, 77 Massachusetts Avenue, Cambridge, Massachusetts 02139, United States

[§] Functional Materials Design, Discovery and Development Research Group, Advanced Membranes and Porous Materials Center, Division of Physical Sciences and Engineering, King Abdullah University of Science and Technology (KAUST), Thuwal 23955-6900, Saudi Arabia

[∥] Materials Science Institute, Department of Chemistry and Biochemistry, University of Oregon, Eugene, Oregon 97403, United States

[⊥] Current address, Institute Charles Gerhardt Montpellier (UMR CNRS 5253), Université Montpellier, Place Eugène Bataillon, 34095, Montpellier, Cedex 05, France

KEYWORDS : 2D, metal-organic frameworks, zirconium MOFs, design, conductivity, electronic properties

Nowadays, zirconium metal–organic frameworks attract more attention due to their robustness and their easier predictability in terms of topology. Herein we have been able to control synthetic parameters in order to construct two new 2D MOFs with the same **sql** topology. Both materials, **ACM-10** and **ACM-11** have been characterized by single crystal X-ray diffraction, thermogravimetric analysis and UV-vis spectroscopy. Their textural, electrochemical and conductivity properties are presented along with the opportunities that these new topologically interesting scaffolds offer for the design of new structures.

Over the past two decades, metal-organic frameworks (MOFs) have garnered attention due to their structural and compositional tunability, resulting in low-density crystalline solids. Their high porosity has positioned them for applications in gas storage, [1-4] separations, [5-7] or catalysis. [8-10] More recently, MOFs have been studied as potential high-surface area electrodes in electrical devices [11,12] (*e.g.* chemiresistive sensors, [13,14] electrochemical catalysts [15]). The success of MOFs in these applications depends on the electrical conductivity of the framework itself. Indeed, most MOFs are electrical insulators: charge carrier mobility is typically inversely proportional to crystal density, and many frameworks feature insulating metal-oxide ionic interfaces. To improve the conductivity of MOFs, several strategies have been developed; the most successful installs charge carriers through chemical redox of either the metal/node or ligand. [16-20]

However, chemical stability of the framework is another critical property required for electrically conductive MOF applications. Examination of the literature reveals that frameworks featuring confined ceramic nodes (*e.g.* the UiO-[21,22] and NU-series, [23]and other $Zr_6(O)4(OH)4$ containing frameworks) boast improved chemical stability over their late transition metal analogues. [21-25] Zr-based frameworks are known, however, to be primarily electrically insulating even with the inclusion of electroactive guests into the pores. [26,27] Inspired by both the pursuit of a chemically stable and redox active scaffold, we aimed to synthesize novel Zr-based frameworks composed of redox active linkers.

Previous studies have shown that tetrathiafulvalene (TTF) may be singly and doubly oxidized to form stable radical and aromatic adducts, respectively. [28,29] The explicit one-electron oxidation results in the formation of a hole,

i.e. p-type charge carriers. Electrical conduction is then determined by the extent of the hole delocalization throughout the material, a process that is typically governed by inter TTF-TTF π-stacking interactions. With this in mind, TTF-containing ligands (*e.g.,* tetrathiafulvalene tetrabenzoic acid, TTFTB) have been incorporated into MOFs. [17,30-35] The resultant materials were shown to be modest electrical conductors, [36-40] with the highest performing materials featuring closely packed TTF subunits repeating throughout the crystal.

In contrast, there are a series of materials featuring isolated redox active linkers (rather than π-stacked chains) that still exhibit ligand oxidation. [33,38] In these cases the oxidation-generated hole is localized, as evidenced by electronic structure calculations and electrical conductivity measurements. While not conductive, these materials are still interesting as they offer unique routes to storing holes in relatively high concentrations (*i.e.* up to one per ligand) thereby enabling these frameworks to be potentially interesting catalysts. [41, 42, 43]

Considering these motivations, the combination of a Zr-based $Zr_6(O)4(OH)4$ node with a redox active ligand is an attractive platform because the resultant scaffold may feature interesting conductive properties and/or ligand-centered redox chemistry, as well as affording opportunities to install catalytic metals onto/into the Zr-node**.** [44] TTFTB shares similar topology to its pyrene analogue, one may expect to form a NU-1000 derivative, but privileged with ligand-centered redox activity. However, upon examination of ~40 Zr-based MOFs built from quasi-planar tetratopic linkers the resultant topology depends on whether the Zr-clusters are 12-, 8- or 6- connected (resulting in 4,12-c **ftw**/**shp**, 4,8-c **csq**/**sqc**/**scu**, and 4,6-c **she**, respectively), which itself depends on the synthetic conditions. [45-47]

The assembly of a single crystal Zr-TTFTB containing framework is challenging as there is competition between formation of the strong Zr-carboxylate bond and the π-stacking of the ligands, particularly if the ligands are partially oxidized during synthesis. In this work, through control of the synthetic conditions, we report two crystal structures of Zr-TTFTB, **ACM-10** and **ACM-11**. Both frameworks are 2D connected, and are characterized by single crystal X-ray diffraction, thermogravimetric analysis and UV-vis spectroscopy. Their structural, electrochemical and conductivity properties are presented, as well as opportunities afforded by these new topologically interesting scaffolds.

Experimental

All chemicals were acquired from commercial sources and used as obtained. H_4TTFTB was ordered from Chemsoon. Reagent grade solvents were used.

Synthesis of **ACM-10**, $[Zr_6O_4(OH)_4(H_2O)_2(TTFTB)_2(HCOO)_4]\cdot 11.4DMF\cdot 3H_2O$.

In a pyrex vial, H_4TTFTB (4.6 mg, 0.007 mmol) was dissolved in a mixture of DMF-H_2O (1 mL-0.25 mL) in the presence of formic acid (0.76 mL). Then 40 μL of a $ZrOCl_2$ solution 0.5 M in water was added. The solution was sonicated few minutes before being placed in a preheated oven at 115˚C for 3 days. After cooling down, orange polycrystalline powder was recovered by filtration, washed with acetonitrile and dried in air. Orange diamond shaped crystals were obtained using 1 mL of formic acid (Figure S1). The yield, based on zirconium, is 39.4 %. Elemental analysis: theoretical N= 5.06%, C = 40.53%, H = 3.93%, S = 8.15% and experimental N= 4.7047%, C = 40.8335%, H = 3.4132%, S = 9.1421%.

Synthesis of **ACM-11**, $[Zr_6(O)_4(OH)_4(H2O)_8(TTFTB)_3]\cdot 7.6DMF$.

In a pyrex vial, H_4TTFTB (6.8 mg, 0.01 mmol) was dissolved in a DEF (1 mL) in the presence of formic acid (0.57 mL). Then 40 μL of a $ZrOCl_2$ solution 0.5 M in water was added. The solution was sonicated few minutes before being placed in a preheated oven at 115˚C for 3 days. After cooling down, dark red square crystals were recovered by filtration, washed with acetonitrile and dried in air (Figure S1). The yield, based on zirconium is 62.2 %. Elemental analysis: theoretical N= 3.11%, C = 43.77%, H = 3.54%, S = 11.21% and experimental N= 2.89%, C = 43.51%, H = 3.48%, S = 11.71%

CCDC 1910185, 1910226 contain the supplementary crystallographic data for this paper. These data can be obtained free of charge from the Cambridge Crystallographic Data Centre via www.ccdc.cam.ac.uk. Selected crystal data and details on structure determinations are listed in Table 1

Powder X-ray diffraction (PXRD). PXRD measurements were carried out at room temperature on a Bruker D8 Advance X-ray diffractometer with Cu Kα radiation (λ= 0.154 nm) operated at 40 kV and 40 mA in a Bragg–Brentano geometry with a scan speed of 1s/step and a step size of 0.02˚. For the longer PXRD measurements necessary for LeBail fit, we used a scan speed of 3s/step and a step size of 0.02˚.

Single crystal structure analysis (SCXRD).

Single crystal X-Ray data were collected using a Bruker X8 PROSPECTOR APEX2 CCD diffractometer using CuKα radiation (λ = 1.54178 Å). Indexing was performed using APEX2 (Difference Vectors method).[48] Data integration and reduction were performed using SaintPlus 6.01. [49] Absorption correction was performed by multi-scan method implemented in SADABS. [50] Space groups were determined using XPREP implemented in APEX2.[51] Structures were solved using Direct Methods (SHELXS-97) and refined using SHELXL-2018/3 [52] (full-matrix least squares on F^2) contained WinGX v1.70.01.[53]

Elemental analysis. Elemental analysis data were obtained from a ThermoFinnigan apparatus.

Thermogravimetric analysis (TGA). Thermal analyses were conducted on a Mettler Toledo, Thermo Scientific instrument (Model TGA/DSC1, Nicolet iS10). Around 3 mg of sample was submitted to an air flow of 30 mL/min and heated until 900˚C at a rate of 2˚C/min.

Adsorption analysis. N2 sorption experiments were performed on a fully automated Quadrasorb SI (Quantachrome Instruments) at relative pressures up to 1 atm. The cryogenic temperatures were controlled using

liquid nitrogen bath at 77 K. Samples were exchanged with acetonitrile for 3 days prior experiments, then degassed over night at room temperature under vacuum.

Cyclic voltammetry (CV). The CV of solid-state compounds were tested in a conventional three electrodes electrochemical set-up using Pt wire as the counter electrode and Ag/AgCl (sat'd KCl) as the reference electrode. The CV's were performed at room temperature (298 K) using a 16-channel, research-grade potentiostat system (VMP3; Bio-Logic Science Instruments). The working electrode was Pt sputtered onto glass, then, dry material was pressed on the surface, followed by few drops of an ethanol-nafion (1:1) mixture and let dried at room temperature for 15h.

Conductivity measurements. Powders were dried under dynamic vacuum for 3 hours. Using a home-built two-probe *in situ* press set-up described previously, [37] two-contact probe measurements were carried out at 296 K in ambient atmosphere on pressed pellets. Linear *I–V* curves were obtained by sweeping the voltage between –0.5 and +0.5 V, and measuring the current using a sourcemeter (Keithley 2450).

Optical microscope. To determine morphology the materials, Leica DM750 optical microscope equipped with a camera MC170 HD was used.

Diffuse Reflectance UV/vis Spectroscopy. The optical properties were obtained by using a JASCO V-670 spectrophotometer equipped with an integrating sphere. The diffuse reflectance spectra were recorded in range of 200-800 nm using halogen and deuterium lamps as light sources. The obtained data were processed using Kubelka – Munk function.

Calculations. Beginning with the experimentally obtained crystal structure for **ACM-10**, quantum chemical simulations were performed using the DFT framework as implemented in VASP, [54] a commercial software package. The framework was geometrically equilibrated using the PBEsolfunctional with a Gamma-only k-grid, and a 500 eV planwave cutoff. [55] Convergence criteria were set to <0.005 eV per atom. The electronic band structures were then obtained using the PBEsol geometry computed with the HSE06functional, [56] sampling five equally spaced low symmetry k-points along high symmetry vectors. The electron energies were then aligned to the vacuum level using MacroDensity.[57] **ACM-11** was not computed due to the size of the unit cell and the subtle potential energy surface associated with the H-bonding Zr-bound hydrates.

ACM-10 postsynthetic modification. ACM-10 was grafted with Ti(IV) by a method previously reported.[58] All manipulations were performed inside glovebox under argon atmosphere. Typically, 30 mg ACM-10 was mixed with 2 mL DMF inside 10 mL vial. Then 3.38 µmol $Ti(O^tBu)_4$ were added, and mixture was transferred to preheated oven at 100°C for 24 h. The powder was isolated by centrifugation and washed with DMF, followed by soaking in MeOH for 3 days. Finally, powder was filtered and dried at 160°C for 4 h.

Photocatalytic measurements. The photocatalytic hydrogen production experiments were performed in a quartz batch reactor at continuous Ar flow (2 mL min^{-1}). Samples (ACM-10 and Ti-grafted ACM-10) 20 mg were suspended in 20 mL aqueous solution of L-ascorbic acid (0.1 M) with the addition of H_2PtCl_6 as cocatalyst (3.5 wt. % Pt). The suspension was purged with argon prior to photoirradiation by 300 W Xenon lamp (320-775 nm) or Xenon coupled with cut-off filter (λ≥380 nm, HOYA L38). The amount of evolved H_2 was measured by gas chromatography (Shimadzu Model GC-8A, TCD, Ar gas, molecular sieve 5A).

Results and discussion

The use of formic acid as a monotopic modulator resulted in the isolation of two 2D-connected frameworks; **ACM-10** and **ACM-11.** Both crystallize in very similar conditions; in fact our first syntheses led to a mixture of both compounds. However, we later discovered that **ACM-10** can be obtained as a pure phase by adding a small amount of water to the synthesis mixture. Purities of both phases were assessed by Le Bail fits of the PXRD patterns (Figure S2 and S3) and elemental analysis. Single crystals of **ACM-10,** an orange crystalline powder, were obtained using high concentrations of modulator. Initially 0.75 mL was used in order to avoid any risk of excess pressurization. Increasing to 1 mL of formic acid yielded orange single crystals. Complementarily, the use of DEF instead of DMF and lower concentration of formic acid led to phase-pure red-brown single crystals of **ACM-11**. Both materials where simplified using the topology rules in a similar way as the convention applied for zeolite. This analysis reveals a **sql** topology (sql means square lattice) where each cluster is connected to four independent ligands. The difference between the two phases, however, arises from the degree of cluster hydration: in **ACM-10** each linker connects to four different clusters while in **ACM-11** half of linkers are connected to four independent clusters and the other half are linked to two independent cluster and have two pendant carboxylates partaking in H-bonding to node-bound water. A similar coordination environment was observed for MgTTFTB.[38]

Single crystal X-ray diffraction reveals that **ACM-10** crystallizes in a monoclinic system in the space group *P*2/*m*. Each of the six Zr(IV) cations are surrounded by eight oxygen donors, resulting in a hexanuclear cluster (Figure 1A). Four Zr(IV) are bound to two μ_3-OH and two μ_3-O anions, two oxygen atoms from deprotonated carboxylate groups of two independent ligands, one oxygen atom from one deprotonated formate molecule and one oxygen from either a water molecule or a formate anion. The two other Zr(IV) cations are surrounded by four μ_3-OH/O groups and four oxygen atoms from carboxylate groups of four independent TTFTB. This results in a molecular building block (MBB) formula of $Zr_6(\mu_3\text{-}O)_4(\mu_3\text{-}OH)_4(H_2O)_2(\text{-}O_2C)_8(\text{-}O_2C)_4$.

Table 1. Selected Crystal Data and Details on Structure Determinations from SCXRD Analysis

	ACM-10	ACM-11

Empirical formula	$C_{106.14}H_{129.66}N_{11.38}O_{48.38}S_8Zr_6$	$C_{147.78}H_{174.82}N_{15.26}O_{55.26}S_{12}Zr_6$
Formula weight	3142.74	3981.04
Crystal system	Monoclinic	Orthorhombic
Space group	*P*2/*m*	*Cccm*
Unit cell dimensions	a = 11.9579(7) Å, b =13.1129(8) Å, c = 20.925(1) Å, β = 98.672(2)°	a = 15.1339(8) Å, b =27.942(2) Å, c = 42.169(2)Å,
Volume	3243.5(3) Å^3	17832(2)Å^3
Z, calculated density	1, 1.609 Mg m^{-3}	4, 1.483 Mg m^{-3}
F(000)	1601	8170
Temperature (K)	130.0(1)	296(2)
Radiation type, λ	Cu $K\alpha$, 1.54178 Å	Cu $K\alpha$, 1.54178 Å
Absorption coefficient	5.79 mm^{-1}	4.81 mm^{-1}
Absorption correction	Multi-scan	Multi-scan
Max and min transmission	0.753 and 0.547	0.127 and 0.048
Crystal size	0.02 × 0.03 × 0.03 mm	0.03 × 0.04 × 0.04 mm
Shape, colour	Prism, orange	Prism, red-brown
θ range for data collection	3.4–50.5°	2.1–47.2°
Limiting indices	$-11 \le h \le 11$, $-13 \le k \le 13$, $-20 \le l \le 20$	$-14 \le h \le 14$, $-26 \le k \le 26$, $-40 \le l \le 40$
Reflection collected / unique / observed with $I > 2\sigma(I)$	38895 / 3583 (R_{int} = 0.041) / 3247	68422 / 4128 (R_{int} = 0.105) / 2608
Completeness to θ_{max} = 50.5°	99.7 %	100.0 %
Refinement method	Full-matrix least-squares on F^2	Full-matrix least-squares on F^2
Data / restraints / parameters	3583 / 166 / 386	4128 / 391 / 364
Final R indices [$I > 2\sigma(I)$]	R_1 = 0.049, wR_2 = 0.136	R_1 = 0.073, wR_2 = 0.219
Final R indices (all data)	R_1 = 0.053, wR_2 = 0.139	R_1 = 0.105, wR_2 = 0.254
Weighting scheme	$[\sigma^2(F_o^2)+ 0.079P)^2 + 16.3732P]^{-1*}$	$[\sigma^2(F_o^2)+(0.1482P)^2 +129.9137P]^{-1*}$
Goodness-of-fit	1.06	1.05
Largest diff. peak and hole	1.61 and -0.80 e Å^{-3}	1.05 and -0.71 e Å^{-3}

$^*P = (F_o^2 + 2F_c^2)/3$

One MBB is connected to eight independent TTFTB ligands, and each TTFTB link four independent hexanuclear clusters. The final 2D framework features infinite sheets in the *bc* plane (Figure 1B and 1C). The topological analysis shows a double **sql** layer constructed from the bridged hexanuclear cluster where carbon atoms of the coordinated carboxylates, acting as points of extension, coincide with the vertices of the square figure of the **sql** net and TTFTB acts as the 4-c node (Figure 1D).

Three types of porous channels can be distinguished in **ACM-10**. Two along the *a* axis that exhibit an aperture size of 6.6 Å and 3 Å, after formate removal, and one along the *b* axis with an aperture of 5.4 Å. The two ligands on both sides, above and below the hexanuclear cluster, present a maximal distance between planes of two tetrathiafulvalene cores (>S_2C=CS_2<) of 8.67(1) Å leading to porous channel along the *b* axis. However, between two layers, π–π stacking exists with a short plane- to-plane distance of 3.25(1) Å between two ligands. Along the *a* direction, the hexanuclear clusters are linked *via* strong hydrogen bonding between the water molecules and formate anions with donor-to-acceptor distances of 2.61(1) Å.

ACM-11 crystallizes in the space group *Cccm* with an orthorhombic crystal system. As in **ACM-10**, the inorganic node is built from six Zr(IV) cations to form an hexanuclear cluster (Figure 1A). Two Zr(IV) cations are surrounded by four oxygen atoms from deprotonated carboxylate groups of four independent ligands and by two μ_3-OH and two μ_3-O anions each. Each other four Zr(IV) cations possess two μ_3-O anions, two μ_3-OH, two oxygen atoms from two carboxylate group belonging to two independent TTFTB and two oxygens from two water molecules in their coordination sphere.

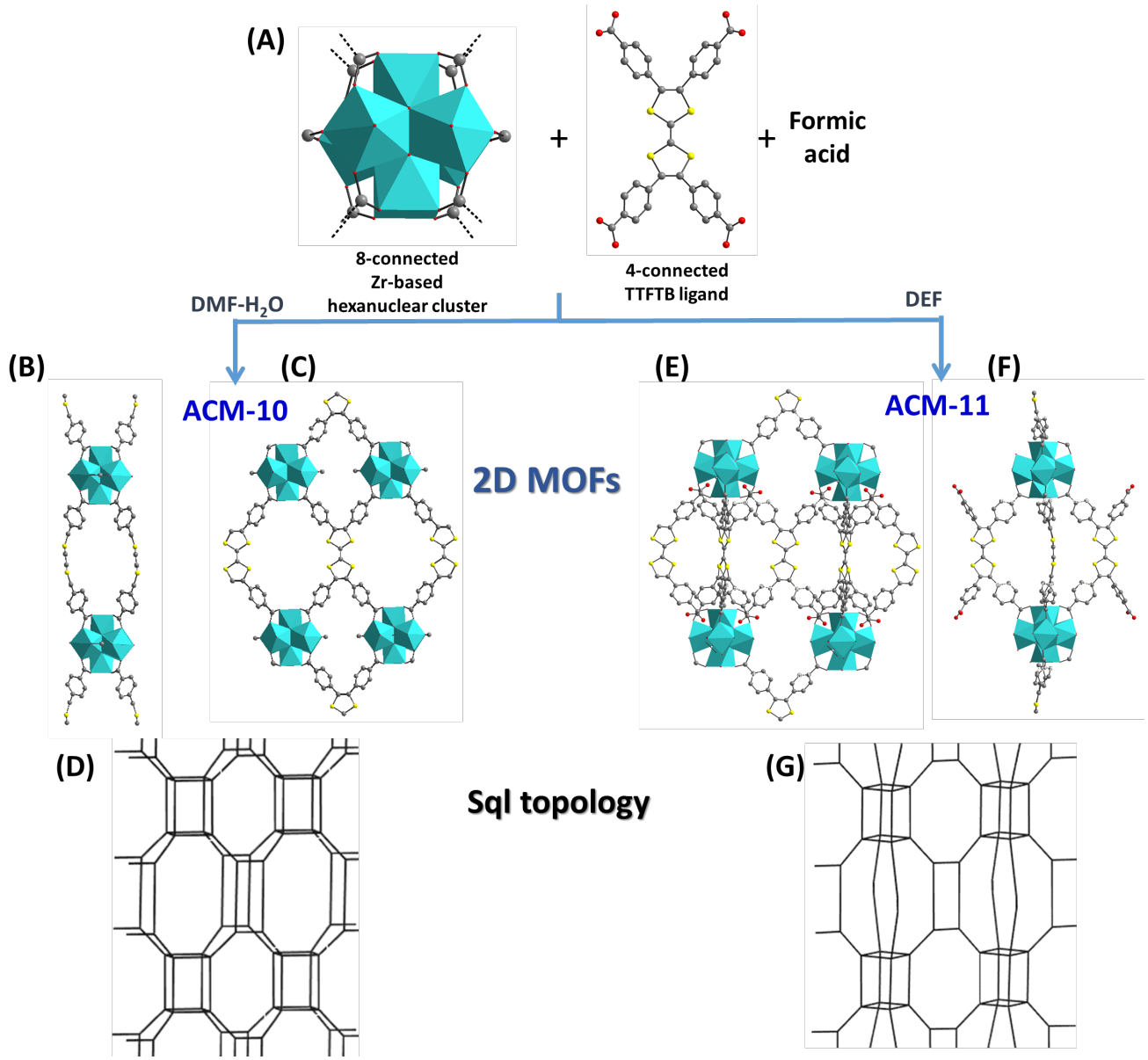

Figure 1. Synthetic path and crystal structures of the two new 2D-ZrMOFs. (A) Building blocks used for the synthesis: 8-connected inorganic hexanuclear zirconium cluster and 4-connected organic ligand TTFTB building block (B) One layer of **ACM-10**, view along the *b* axis highlighting the double layer (C) Crystal structure of **ACM-10** view along the *a* axis (D) representation of the **sql** topology of **ACM-10**(E) Crystal structure of **ACM-11** view along the *b* axis (F) One layer of **ACM-11** view along the *a* axis highlighting the decorated TTFTB ligand (G) representation of the **sql** topology of **ACM-11**.

ACM-11 displays a similar 2D framework with **sql** topology, with infinite sheet connectivity in the *ac* plane (Figure 1G). **ACM-11** can be described as a **sql** layer where the hexanuclear cluster and the TTFTB ligand act as 4-connected nodes (Figure 1E). This layer is further decorated by two ligands in the perpendicular direction, *b* (Figure 1F). These decorative TTFTB ligands exhibit two pendant carboxylates that are hydrogen-bonded to the water molecule of the hexanuclear cluster from the neighbor sheet. **ACM-11** exhibits two kinds of cavities: channels along the axis *a* with an aperture size estimated around 5 Å and cages. Cages have an octahedral shape where two vertexes are Zr_6 cluster and the tetrathiafulvalene core can be viewed as the other four vertexes. An aperture of 6.2 Å gives access to the cage which exhibit an internal diameter of 9 Å. Here, the shortest distance between two ligands from two neighbor layers is 6.97 Å. The shortest S···S contact distance is 4.89 Å, located between two perpendicular ligands. Both **ACM-10** and **ACM-11** feature multiple node-based sites that could play host to extrinsic metals. The metal-appendage approach has been widely used for other Zr-containing scaffolds, [59] but here the topology and MBB privilege both structures with the additions of potentially higher metal loadings.

One of our key targets in this work was to synthesize an electronically interesting, stable, MOF. We first evaluated the stability of **ACM-10** and **ACM-11**, the bulk materials were immersed in acetonitrile and water for 24h. The PXRD pattern of **ACM-10** shows no changes compared to the as-synthesized sample, confirming that its structure is

not affected. **ACM-11** was less stable in water as evidenced by the broadening of the peaks (Figure S4 and Figure S5).

The thermal stability of **ACM-10** and **ACM-11** was evaluated using thermal gravimetric analysis (TGA) on the as-synthesized samples. Accordingly, the TGA curves exhibit a first weight loss between 100 ˚C and 400 ˚C and 100 ˚C and 300 ˚C for **ACM-10** and **ACM-11**, respectively, corresponding to solvent departure (Figure S9 and Figure S10). Mass losses are in good agreement with formula as experimental and theoretical loss values are 28.1% and 27.7% and 18.8% and 20.5%, for **ACM-10** and **ACM-11,** respectively. At temperatures exceeding 400 ˚C for **ACM-10** and 300 ˚C for **ACM-11**, significant weight reductions are observed and are associated with framework decomposition. The structure analysis combined with TGA supports the presence of permanent microporosity. The nitrogen adsorption-desorption isotherm is presented Figure S11. The apparent specific Brunauer–Emmett–Teller (BET) surface areas are estimated to be 380 m^2/g and 420 m^2/g for **ACM-10** and **ACM-11**, respectively. The associated pore volume of **ACM-10** is 0.18 cm^3/g (theoretical PV = 0.17 cm^3/g) while the pore volume of **ACM-11** is 0.25 cm^3/g (theoretical PV = 0.23 cm^3/g).

Electronically, both MOFs have visible absorption features. However, the emergence of color is usually orthogonally related to the conductivity of the framework. UV-vis spectra after Kubelka–Munk transformation are presented in Figure S6. As expected, a significant red shift is observed for **ACM-11** compared to **ACM-10**. Indeed **ACM-10** has a bright orange color whereas **ACM-11** present dark red crystal (Figure S1). *Tauc* plots (used to extract bandgaps) are shown in Figure S6. From this figure, the estimated bandgaps are ~2.16 eV for **ACM-10** and ~1.9 eV for **ACM-11** (Figure S7 and Figure S8). Most colored MOFs also feature discretized electron energy levels. Explicit ligand redox can typically be probed using electrochemical measurements. Cyclic voltammograms (CVs) were performed in acetonitrile with 0.1 M tetrabutylammonium hexafluorophosphate and 2 mg of ferrocyanide and are shown in Figure 2. Using a Pt electrode only the reversible oxidation/reduction of $Fe^{2+/3+}$ at 0.5 V *vs*. Ag/AgCl is observed. The tetrathiafulvalene (TTF) core is known to undergo sequential and reversible oxidations from TTF to the radical cation ($TTF^{+\bullet}$) followed by the dication (TTF^{2+}). However, only one large cathodic current was observed for **ACM-10** and **ACM-11**. Both materials showed a large cathodic current from 0 V to –1.5 V vs. Ag/AgCl. This peak was irreversible after the first CV and no corresponding anodic peak was observed (Figure S12). This large cathodic current was ascribed to the reduction of the TTFTB in the MOF.

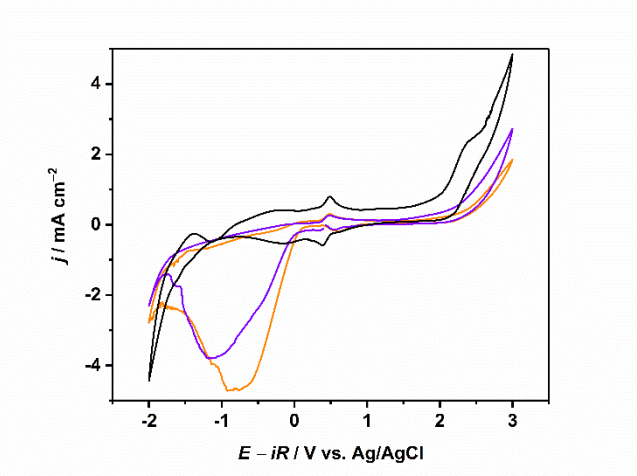

Figure 2. First cyclic voltammograms curve (50 mV s^{-1}) for **ACM-10** (orange) and **ACM-11** (purple) in acetonitrile. Platinum for reference is in black

To investigate the electrical conductivity of **ACM-10** and **ACM-11**, the *I–V* curves of two-contact probe pressed pellet devices were measured for three different batches of each material (Figures S13-S15). **ACM-10** exhibited an average conductivity of $3(2) \times 10^{-10}$ S/cm, with a champion value of $1.3(2) \times 10^{-9}$ S/cm. **ACM-11** exhibited slightly higher conductivities, with an average value of $6(2) \times 10^{-9}$ S/cm and a champion value of $1.8(2) \times 10^{-8}$ S/cm. The lower conductivity of **ACM-10** and **ACM-11** compared to other frameworks based on TTFTB can be attributed to the absence of continuous π-stacking among the TTF moieties in the structure.[35,40] Nevertheless, these conductivity values indicate that intermolecular charge transfer (i.e. hopping) among the ligands is energetically accessible at ambient temperatures, consistent with the crystallographic contact distances.

While the electrical conductivity is less than desired for sensing and capacitive technologies, quantum chemical simulations reveal unique opportunities for **ACM-10** (see Figure 3). Unlike other Zr-containing framework, **ACM-10** features a narrow electronic band gap (computed to be 1.7 eV, in reasonable agreement with experimental data), arising from transitions between relatively high energy TTF-centered and TB-centered orbitals. These high energy electrons are readily liberated (*i.e.* TTFTB is oxidized), resulting in depletion of the valence band. In principle these holes would then move through the material, but here these TTFTB orbitals do not overlap in the crystal (the origin of low conductivity in this case). Meanwhile, the conduction band is relatively dispersed, with comparable electron affinity energetics to the UiO-series,[60] suggesting that similar post-synthetic modification routes may provide access to a chemically stable, *visible light absorbing*, catalytic scaffold. For example, one fruitful approach has been through the deposition of Ti^{4+} onto the surface of the Zr-nodes. Such approaches did yield catalytic variants of UiO-type materials;[58] their shortcoming has always been the wide electronic band gap and reliance on metals being appended to linker vacant sites. Here, **ACM-10** boasts multiple coordination sites for extrinsic metals, desirable band

gap, and ideal chemical stability, making this material compelling for future photocatalytic studies.

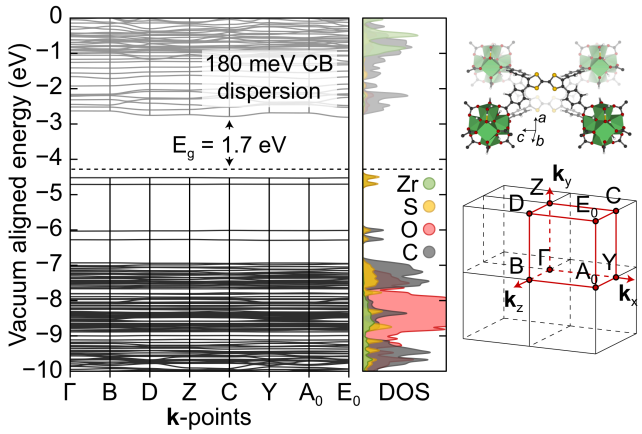

Figure 3. The electronic band structure of **ACM-10**. The electronic band gap matches the red/orange color observed in synthesis. The valence band is composed of highly localized TTFTB-centered orbitals, in line with the diminished TTFTB π-stacking in the crystal. The conduction band features surprisingly disperse bands, attributed to delocalized π electrons in the ligand anti-bonding orbitals.

Thus, in order to demonstrate advantages of coordination sites, band gap value and chemical stability of ACM-10 for photocatalytic activity we performed postsynthetic modification of ACM-10 by Ti(IV) incorporation through the treatment of ACM-10 with Ti(O^tBu)$_4$ (Figure S). Ti-grafted ACM-10 with 0.06/1 Ti/Zr atom ratio exhibits 5.2- and 10.8- times improved activity in HER (0.6 and 1.59 μmol h^{-1}) under visible-light and UV+Vis irradiation respectively compare to pristine ACM-10 (Figure 4). Stability was confirmed with PXRD (Figure S16).

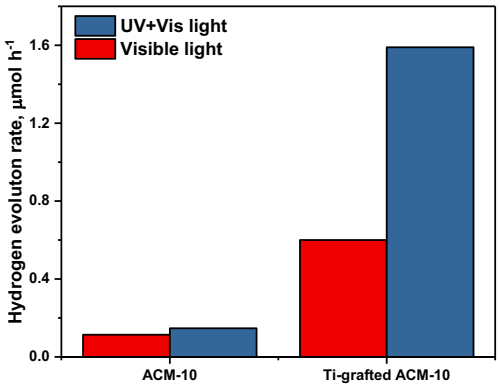

Figure 4. Photocatalytic activity of ACM-10 and Ti-grafted ACM-10 in hydrogen production under Visible (λ≥380 nm) and UV+Vis light (320-775 nm).

Conclusions

By combining an 8-conneced Zr cluster with the tetratopical ligand TTFTB we synthesized two new Zr based 2D metal organic frameworks. ACM-10 and ACM-11 share a Sql topology that expands in two dimensions and isolate the redox linker at different interplanar distances. The electrical conductivities of ACM-10 and ACM-11, while relatively low, indicate that some charge hopping among the electroactive TTF units is energetically accessible. ACM-10, in particular, is predicted to have a large potential for photocatalytic applications, with multiple coordination sites for extrinsic metals, a desirable band gap, and an ideal chemical stability what was experimentally confirmed in photocatalytic hydrogen evolution reaction.

ASSOCIATED CONTENT

Supporting Information. Optical images, Le Bail Fit, PXRD, UV-vis, TGA, CV and I-V curves are available free of charge via the Internet at http://pubs.acs.org."

AUTHOR INFORMATION

Corresponding Author

* **jorge.gascon@kaust.edu.sa**

Author Contributions

The manuscript was written through contributions of all authors. All authors have given approval to the final version of the manuscript.

Funding Sources

The work at MIT was supported by the U.S. Department of Energy, Office of Science, Office of Basic Energy Sciences (DE-SC0018235). L.S.X. and S.S.P. thank the National Science Foundation for support through the Graduate Research Fellowship Program (1122374). A.C. thanks the program P.I.A "MOPGA" (APPAT) for funding.

REFERENCES

(1) Li, H.; Wang, K.; Sun, Y.; Lollar, C. T.; Li, J.; Zhou, H.-C. Recent advances in gas storage and separation using metal–organic frameworks. *Materials Today* **2018,** *21* (2), 108.

(2) Jiang, J.; Furukawa, H.; Zhang, Y.-B.; Yaghi, O. M. High Methane Storage Working Capacity in Metal–Organic Frameworks with Acrylate Links. *Journal of the American Chemical Society* **2016,** *138* (32), 10244.

(3) Gygi, D.; Bloch, E. D.; Mason, J. A.; Hudson, M. R.; Gonzalez, M. I.; Siegelman, R. L.; Darwish, T. A.; Queen, W. L.; Brown, C. M.; Long, J. R. Hydrogen Storage in the Expanded Pore Metal–Organic Frameworks M2(dobpdc) (M = Mg, Mn, Fe, Co, Ni, Zn). *Chemistry of Materials* **2016,** *28* (4), 1128.

(4) Bourrelly, S.; Llewellyn, P. L.; Serre, C.; Millange, F.; Loiseau, T.; Férey, G. Different Adsorption Behaviors of Methane and Carbon Dioxide in the Isotypic Nanoporous Metal Terephthalates MIL-53 and MIL-47. *Journal of the American Chemical Society* **2005,** *127* (39), 13519.

(5) Cadiau, A.; Adil, K.; Bhatt, P. M.; Belmabkhout, Y.; Eddaoudi, M. A metal-organic framework–based splitter for separating propylene from propane. *Science* **2016,** *353* (6295), 137.

(6) Adil, K.; Belmabkhout, Y.; Pillai, R. S.; Cadiau, A.; Bhatt, P. M.; Assen, A. H.; Maurin, G.; Eddaoudi, M. Gas/vapour separation using ultra-microporous metal–organic frameworks: insights into the structure/separation relationship. *Chemical Society Reviews* **2017,** *46* (11), 3402.

(7) Cadiau, A.; Belmabkhout, Y.; Adil, K.; Bhatt, P. M.; Pillai, R. S.; Shkurenko, A.; Martineau-Corcos, C.; Maurin, G.; Eddaoudi, M. Hydrolytically stable fluorinated metal-organic frameworks for energy-efficient dehydration. *Science* **2017,** *356* (6339), 731.

(8) Rogge, S. M. J.; Bavykina, A.; Hajek, J.; Garcia, H.; Olivos-Suarez, A. I.; Sepúlveda-Escribano, A.; Vimont, A.; Clet, G.; Bazin, P.; Kapteijn, F.et al. Metal–organic and covalent organic frameworks as single-site catalysts. *Chemical Society Reviews* **2017,** *46* (11), 3134.

(9) Xu, C.; Fang, R.; Luque, R.; Chen, L.; Li, Y. Functional metal–organic frameworks for catalytic applications. *Coordination Chemistry Reviews* **2019,** *388*, 268.

(10) Drout, R. J.; Robison, L.; Farha, O. K. Catalytic applications of enzymes encapsulated in metal–organic frameworks. *Coordination Chemistry Reviews* **2019,** *381*, 151.

(11) Xu, Y.; Li, Q.; Xue, H.; Pang, H. Metal-organic frameworks for direct electrochemical applications. *Coordination Chemistry Reviews* **2018,** *376*, 292.

(12) Stassen, I.; Burtch, N.; Talin, A.; Falcaro, P.; Allendorf, M.; Ameloot, R. An updated roadmap for the integration of metal–organic frameworks with electronic devices and chemical sensors. *Chemical Society Reviews* **2017,** *46* (11), 3185.

(13) Campbell, M. G.; Sheberla, D.; Liu, S. F.; Swager, T. M.; Dincă, M. Cu3(hexaiminotriphenylene)2: An Electrically Conductive 2D Metal–Organic Framework for Chemiresistive Sensing. *Angewandte Chemie International Edition* **2015,** *54* (14), 4349.

(14) Campbell, M. G.; Liu, S. F.; Swager, T. M.; Dincă, M. Chemiresistive Sensor Arrays from Conductive 2D Metal–Organic Frameworks. *Journal of the*

American Chemical Society **2015,** *137* (43), 13780.

(15) Liao, P.-Q.; Shen, J.-Q.; Zhang, J.-P. Metal–organic frameworks for electrocatalysis. *Coordination Chemistry Reviews* **2018,** *373*, 22.

(16) D'Alessandro, D. M. Exploiting redox activity in metal–organic frameworks: concepts, trends and perspectives. *Chemical Communications* **2016,** *52* (58), 8957.

(17) Su, J.; Yuan, S.; Wang, H.-Y.; Huang, L.; Ge, J.-Y.; Joseph, E.; Qin, J.; Cagin, T.; Zuo, J.-L.; Zhou, H.-C. Redox-switchable breathing behavior in tetrathiafulvalene-based metal–organic frameworks. *Nature Communications* **2017,** *8* (1), 2008.

(18) Li, P.; Wang, B. Recent Development and Application of Conductive MOFs. *Israel Journal of Chemistry* **2018,** *58* (9-10), 1010.

(19) Sun, L.; Campbell, M. G.; Dincă, M. Electrically Conductive Porous Metal–Organic Frameworks. *Angewandte Chemie International Edition* **2016,** *55* (11), 3566.

(20) Ko, M.; Mendecki, L.; Mirica, K. A. Conductive two-dimensional metal–organic frameworks as multifunctional materials. *Chemical Communications* **2018,** *54* (57), 7873.

(21) Cavka, J. H.; Jakobsen, S.; Olsbye, U.; Guillou, N.; Lamberti, C.; Bordiga, S.; Lillerud, K. P. A New Zirconium Inorganic Building Brick Forming Metal Organic Frameworks with Exceptional Stability. *Journal of the American Chemical Society* **2008,** *130* (42), 13850.

(22) Kandiah, M.; Nilsen, M. H.; Usseglio, S.; Jakobsen, S.; Olsbye, U.; Tilset, M.; Larabi, C.; Quadrelli, E. A.; Bonino, F.; Lillerud, K. P. Synthesis and Stability of Tagged UiO-66 Zr-MOFs. *Chemistry of Materials* **2010,** *22* (24), 6632.

(23) Islamoglu, T.; Otake, K.-i.; Li, P.; Buru, C. T.; Peters, A. W.; Akpinar, I.; Garibay, S. J.; Farha, O. K. Revisiting the structural homogeneity of NU-1000, a Zr-based metal–organic framework. *CrystEngComm* **2018,** *20* (39), 5913.

(24) Chen, Z.; Hanna, S. L.; Redfern, L. R.; Alezi, D.; Islamoglu, T.; Farha, O. K. Reticular chemistry in the rational synthesis of functional zirconium cluster-based MOFs. *Coordination Chemistry Reviews* **2019,** *386*, 32.

(25) Bai, Y.; Dou, Y.; Xie, L.-H.; Rutledge, W.; Li, J.-R.; Zhou, H.-C. Zr-based metal–organic frameworks: design, synthesis, structure, and applications. *Chemical Society Reviews* **2016,** *45* (8), 2327.

(26) Goswami, S.; Ray, D.; Otake, K.-i.; Kung, C.-W.; Garibay, S. J.; Islamoglu, T.; Atilgan, A.; Cui, Y.; Cramer, C. J.; Farha, O. K.et al. A porous, electrically conductive hexa-zirconium(iv) metal–organic framework. *Chemical Science* **2018,** *9* (19), 4477.

(27) Kung, C.-W.; Otake, K.; Buru, C. T.; Goswami, S.; Cui, Y.; Hupp, J. T.; Spokoyny, A. M.; Farha, O. K. Increased Electrical Conductivity in a Mesoporous Metal–Organic Framework Featuring Metallacarboranes Guests. *Journal of the American Chemical Society* **2018,** *140* (11), 3871.

(28) Canevet, D.; Sallé, M.; Zhang, G.; Zhang, D.; Zhu, D. Tetrathiafulvalene (TTF) derivatives: key building-blocks for switchable processes. *Chemical Communications* **2009**, DOI:10.1039/b818607n 10.1039/b818607n(17), 2245.

(29) Lorcy, D.; Bellec, N.; Fourmigué, M.; Avarvari, N. Tetrathiafulvalene-based group XV ligands: Synthesis, coordination chemistry and radical cation salts. *Coordination Chemistry Reviews* **2009,** *253* (9), 1398.

(30) Qin, Y.-R.; Zhu, Q.-Y.; Huo, L.-B.; Shi, Z.; Bian, G.-Q.; Dai, J. Tetrathiafulvalene–Tetracarboxylate: An Intriguing Building Block with Versatility in Coordination Structures and Redox Properties. *Inorganic Chemistry* **2010,** *49* (16), 7372.

(31) Wang, H.-Y.; Cui, L.; Xie, J.-Z.; Leong, C. F.; D'Alessandro, D. M.; Zuo, J.-L. Functional coordination polymers based on redox-active tetrathiafulvalene and its

derivatives. *Coordination Chemistry Reviews* **2017,** *345*, 342.

(32) Wang, H.-Y.; Ge, J.-Y.; Hua, C.; Jiao, C.-Q.; Wu, Y.; Leong, C. F.; D'Alessandro, D. M.; Liu, T.; Zuo, J.-L. Photo- and Electronically Switchable Spin-Crossover Iron(II) Metal–Organic Frameworks Based on a Tetrathiafulvalene Ligand. *Angewandte Chemie International Edition* **2017,** *56* (20), 5465.

(33) Souto, M.; Romero, J.; Calbo, J.; Vitórica-Yrezábal, I. J.; Zafra, J. L.; Casado, J.; Ortí, E.; Walsh, A.; Mínguez Espallargas, G. Breathing-Dependent Redox Activity in a Tetrathiafulvalene-Based Metal–Organic Framework. *Journal of the American Chemical Society* **2018,** *140* (33), 10562.

(34) Souto, M.; Santiago-Portillo, A.; Palomino, M.; Vitórica-Yrezábal, I. J.; Vieira, B. J. C.; Waerenborgh, J. C.; Valencia, S.; Navalón, S.; Rey, F.; García, H.et al. A highly stable and hierarchical tetrathiafulvalene-based metal–organic framework with improved performance as a solid catalyst. *Chemical Science* **2018,** *9* (9), 2413.

(35) Xie, L. S.; Dincă, M. Novel Topology in Semiconducting Tetrathiafulvalene Lanthanide Metal-Organic Frameworks. *Israel Journal of Chemistry* **2018,** *0* (0).

(36) Narayan, T. C.; Miyakai, T.; Seki, S.; Dincă, M. High Charge Mobility in a Tetrathiafulvalene-Based Microporous Metal–Organic Framework. *Journal of the American Chemical Society* **2012,** *134* (31), 12932.

(37) Sun, L.; Park, S. S.; Sheberla, D.; Dincă, M. Measuring and Reporting Electrical Conductivity in Metal–Organic Frameworks: Cd2(TTFTB) as a Case Study. *Journal of the American Chemical Society* **2016,** *138* (44), 14772.

(38) Park, S. S.; Hendon, C. H.; Fielding, A. J.; Walsh, A.; O'Keeffe, M.; Dincă, M. The Organic Secondary Building Unit: Strong Intermolecular π Interactions Define Topology in MIT-25, a Mesoporous MOF with Proton-Replete Channels. *Journal of the American Chemical Society* **2017,** *139* (10), 3619.

(39) Xie, L. S.; Sun, L.; Wan, R.; Park, S. S.; DeGayner, J. A.; Hendon, C. H.; Dincă, M. Tunable Mixed-Valence Doping toward Record Electrical Conductivity in a Three-Dimensional Metal–Organic Framework. *Journal of the American Chemical Society* **2018,** *140* (24), 7411.

(40) Park, S. S.; Hontz, E. R.; Sun, L.; Hendon, C. H.; Walsh, A.; Van Voorhis, T.; Dincă, M. Cation-Dependent Intrinsic Electrical Conductivity in Isostructural Tetrathiafulvalene-Based Microporous Metal–Organic Frameworks. *Journal of the American Chemical Society* **2015,** *137* (5), 1774.

(41) Saouma, C. T.; Tsou, C.-C.; Richard, S.; Ameloot, R.; Vermoortele, F.; Smolders, S.; Bueken, B.; DiPasquale, A. G.; Kaminsky, W.; Valdez, C. N.et al. Sodium-coupled electron transfer reactivity of metal–organic frameworks containing titanium clusters: the importance of cations in redox chemistry. *Chemical Science* **2019,** *10* (5), 1322.

(42) Saouma, C. T.; Richard, S.; Smolders, S.; Delley, M. F.; Ameloot, R.; Vermoortele, F.; De Vos, D. E.; Mayer, J. M. Bulk-to-Surface Proton-Coupled Electron Transfer Reactivity of the Metal–Organic Framework MIL-125. *Journal of the American Chemical Society* **2018,** *140* (47), 16184.

(43) Chambers, M. B.; Wang, X.; Ellezam, L.; Ersen, O.; Fontecave, M.; Sanchez, C.; Rozes, L.; Mellot-Draznieks, C. Maximizing the Photocatalytic Activity of Metal–Organic Frameworks with Aminated-Functionalized Linkers: Substoichiometric Effects in MIL-125-NH2. *Journal of the American Chemical Society* **2017,** *139* (24), 8222.

(44) Rimoldi, M.; Howarth, A. J.; DeStefano, M. R.; Lin, L.; Goswami, S.; Li, P.; Hupp, J. T.; Farha, O. K. Catalytic Zirconium/Hafnium-Based Metal–Organic Frameworks. *ACS Catalysis* **2017,** *7* (2), 997.

(45) Wang, H.; Dong, X.; Lin, J.; Teat, S. J.; Jensen, S.; Cure, J.; Alexandrov, E. V.; Xia, Q.; Tan, K.; Wang, Q.et al. Topologically guided tuning of Zr-MOF

pore structures for highly selective separation of C6 alkane isomers. *Nature Communications* **2018,** *9* (1), 1745.

(46) Feng, D.; Gu, Z.-Y.; Chen, Y.-P.; Park, J.; Wei, Z.; Sun, Y.; Bosch, M.; Yuan, S.; Zhou, H.-C. A Highly Stable Porphyrinic Zirconium Metal–Organic Framework with shp-a Topology. *Journal of the American Chemical Society* **2014,** *136* (51), 17714.

(47) Lyu, J.; Zhang, X.; Otake, K.-i.; Wang, X.; Li, P.; Li, Z.; Chen, Z.; Zhang, Y.; Wasson, M. C.; Yang, Y.et al. Topology and porosity control of metal–organic frameworks through linker functionalization. *Chemical Science* **2019,** *10* (4), 1186.

(48) Bruker. APEX2, AXS. Inc, Madison, Wisconsin, USA. **2014**.

(49) Bruker. SAINT, AXS. Inc, Madison, Wisconsin, USA. **2014**.

(50) Sheldrick, G. M. SADABS, University of Gottingen, Germany. **2008**.

(51) Sheldrick, G. M. XPREP, Version 2008/2, Brucker AXS, Inc. Madison. **2008**.

(52) Sheldrick, G. M. Crystal structure refinement with SHELXL. *Acta. Cryst.* **2015,** *C71*, 3.

(53) Farrugia, L. J. WingX. *J. Appl. Cryst.* **2012,** *45*, 849.

(54) Kresse, G.; Furthmüller, J. Efficiency of ab-initio total energy calculations for metals and semiconductors using a plane-wave basis set. *Computational Materials Science* **1996,** *6* (1), 15.

(55) Perdew, J. P.; Ruzsinszky, A.; Csonka, G. I.; Vydrov, O. A.; Scuseria, G. E.; Constantin, L. A.; Zhou, X.; Burke, K. Restoring the Density-Gradient Expansion for Exchange in Solids and Surfaces. *Physical Review Letters* **2008,** *100* (13), 136406.

(56) Krukau, A. V.; Vydrov, O. A.; Izmaylov, A. F.; Scuseria, G. E. Influence of the exchange screening parameter on the performance of screened hybrid functionals. *The Journal of Chemical Physics* **2006,** *125* (22), 224106.

(57) Butler, K. T.; Hendon, C. H.; Walsh, A. Electronic Chemical Potentials of Porous Metal–Organic Frameworks. *Journal of the American Chemical Society* **2014,** *136* (7), 2703.

(58) Santaclara, J. G.; Olivos-Suarez, A. I.; Gonzalez-Nelson, A.; Osadchii, D.; Nasalevich, M. A.; van der Veen, M. A.; Kapteijn, F.; Sheveleva, A. M.; Veber, S. L.; Fedin, M. V.et al. Revisiting the Incorporation of Ti(IV) in UiO-type Metal–Organic Frameworks: Metal Exchange versus Grafting and Their Implications on Photocatalysis. *Chemistry of Materials* **2017,** *29* (21), 8963.

(59) Yang, D.; Odoh, S. O.; Wang, T. C.; Farha, O. K.; Hupp, J. T.; Cramer, C. J.; Gagliardi, L.; Gates, B. C. Metal–Organic Framework Nodes as Nearly Ideal Supports for Molecular Catalysts: NU-1000- and UiO-66-Supported Iridium Complexes. *Journal of the American Chemical Society* **2015,** *137* (23), 7391.

(60) Nasalevich, M. A.; Hendon, C. H.; Santaclara, J. G.; Svane, K.; van der Linden, B.; Veber, S. L.; Fedin, M. V.; Houtepen, A. J.; van der Veen, M. A.; Kapteijn, F.et al. Electronic origins of photocatalytic activity in d0 metal organic frameworks. *Scientific Reports* **2016,** *6*, 23676.